Nuclear Science and Techniques (2023) 34:25
https://doi.org/10.1007/s41365-023-01177-4

Research on the influence of quadrupole deformation and continuum effects on the exotic properties of ^{15,17,19}B with the complex momentum representation method

Xue-Neng Cao[1] · Xian-Xian Zhou[1] · Ming Fu[1] · Xin-Xing Shi[2]

Received: 22 September 2022 / Revised: 30 November 2022 / Accepted: 2 December 2022 / Published online: 24 February 2023

Abstract
The properties of exotic nuclei are the focus of the present research. Two-neutron halo structures of neutron-rich ^{17,19}B were experimentally confirmed. We studied the formation mechanism of halo phenomena in ^{17,19}B using the complex momentum representation method applied to deformation and continuum coupling. By examining the evolution of the weakly bound and resonant levels near the Fermi surface, *s*–*d* orbital reversals and certain prolate deformations were observed. In addition, by analyzing the evolution of the occupation probabilities and density distributions occupied by valence neutrons, we found that the ground state of ^{15}B did not exhibit a halo and the ground states of ^{17}B and ^{19}B exhibited halos at $0.6 \leq \beta_2 \leq 0.7$ and $0.3 \leq \beta_2 \leq 0.7$, respectively. The low-*l* components in the valence levels that are weakly bound or embedded in the continuous spectrum lead to halo formation.

Keywords Quadrupole deformation · Resonant states · Complex momentum representation · Halo

1 Introduction

Exotic phenomena, including halos, have attracted considerable interest from physicists [1–4] and are one of the most popular frontier topics in radioactive nuclear beam physics. In isotope chains, with an increase in the neutron number, nuclei near the neutron-rich dripline may remarkably appear as neutron halos. As ^{11}Li was discovered to be an *s*-wave two-neutron ($2n$) halo nucleus [5], the formation of a halo is considered to be a large occupation of low orbital angular momentum ($l = 0, 1$) levels close to the threshold of particle emission in weakly bound systems [6–8]. Research on halo structures, both theoretically and experimentally, is of great importance in understanding the structure of the nucleus.

On the experimental side, extensive research on halo nuclei with small mass numbers has led to a clear understanding of their halo structures; for example, ^{8}B is a proton ($1p$) halo nucleus [9]; ^{6}He [10, 11], ^{11}Li [5, 12], and ^{14}Be [13, 14] are $2n$ halo nuclei; and ^{11}Be [15, 16] is a neutron ($1n$) halo nucleus. Subsequently, ^{22}C, ^{17}B, and ^{19}B were found to be *s*-wave $2n$ halo nuclei with large matter radii [17, 18], a small percentage of *s*-orbital spectroscopic factors [19], and an enhanced electric dipole strength [20], respectively. In the heavier mass region, ^{37}Mg [21] (the heaviest halo nucleus observed thus far) and ^{31}Ne [22] and ^{29}F [23] (the heaviest Borromean nucleus to date) were found to be *p*-wave halos at or near the inversion island by single-neutron ($1n$) removal reactions and reaction cross section measurements, respectively.

On the theoretical side, the search for new $2n$-halo systems [24] and new halo features, such as core–halo shape decoupling [25, 26] and the Efimov state [27, 28], has also attracted considerable interest. It can be seen that valence neutrons predominantly occupy *p* and *s* orbitals, so that correlations between *f*–*p* or *s*–*d* orbitals play an essential role

This work was partially supported by the National Natural Science Foundation of China (Nos. 12205001, 11935001, and 12204001) and the Scientific Research program of Anhui University of Finance and Economics (Nos. ACKYC22080 and ACKYC220801).

✉ Xue-Neng Cao
120210067@aufe.edu.cn

[1] School of Management Science and Engineering, Anhui University of Finance and Economics, Bengbu 233030, China

[2] School of Mechanics and Optoelectronic Physics, Anhui University of Science and Technology, Huainan 232001, China

in the formation of halo phenomena. These strong quadrupole correlations between *f–p* or *s–d* orbitals can drive the system to break spherical symmetry and undergo deformation, allowing the number of single-particle levels with low-*l* components to increase, resulting in abundant halos at the neutron dripline [29]. Specifically, Hove et al. [30] used the example of a medium-heavy nucleus ^{72}Ca and found that the presence of a slight, long-range *s*-wave tail is also sufficient to bring about halos in very weakly bound neutron-rich systems. Therefore, it is necessary to study the effects of quadrupole deformation and continuum effects on the halo structure of exotic nuclei.

In this study, we investigated the neutron halo structures of B isotopes. ^{15}B and ^{17}B neutron halo structures have been reported [31, 32]. For ^{15}B, the 2*n* separation energies (S_{2n}) were 3.747 MeV [33], the quadruple deformation length δ was 1.17 [34], the quadruple deformation parameter β_2 was 0.61 [35], and the percentage of the *s* orbital was 63 % [36].

For ^{17}B, a strong mixing of *s* and *d* waves was observed based on the energy dependence observed by the interaction cross section [37]. Tanihata [24] considered large amplitudes of $2s_{1/2}$ waves for all B isotopes with neutron number $n \geq 8$. For ^{17}B, S_{2n} is 1.37 MeV [38], δ is 1.2 [34], β_2 is ~ 0.6 [39] or 0.56 [35], the neutron skin thickness is 0.51 (0.11) fm [40], and the neutron has a large matter radius [40, 41]. The percentages of *s* orbital in ^{17}B are 36(19)% [31], 69(20)% [32], 50(10)% [37], and 53(21)% [42], respectively. In 2021, Yang et al. [19] obtained spectral factors for the $1s_{1/2}$ and $0d_{5/2}$ orbitals, with the $1s_{1/2}$ orbitals contributing only 9(2)% of the spectral factor, which is much smaller than the values given in Refs. [31, 42], revealing that ^{17}B has a well-defined, but not dominant, neutron halo. The structure of this weak halo has been explained by the deformed relativistic Hartree–Bogoliubov theory in the continuum (DRHBc) [19], indicating the significance of deformation effects.

^{19}B is the heaviest bound nucleus of the B isotopes, and, because ^{18}B is unbound, ^{19}B is the Borromean nucleus, suggesting a 2*n* halo structure. ^{19}B has a particularly low two-neutron separation energy (S_{2n}) of $0.089^{+0.560}_{-0.089}$ MeV [38], enhanced interaction cross section [31], and large deformation [35, 43, 44]. Direct mass measurements revealed that the valence neutrons of ^{19}B are dominated by *d* waves, which suppress halo formation [31, 42, 45]. However, Cook et al. [20] found a significant 2*n* halo in ^{19}B using Coulomb dissociation. Recently, ^{19}B has been suggested as a deformed 2*n* halo candidate with shape-decoupling effects [35]. The structures of ^{19}B are also related to the newly discovered unbound isotopes ^{20}B and ^{21}B.

However, the deformation of B isotopes close to the neutron dripline has not been experimentally determined. The shape of the nucleus is determined by the shell structure of protons and neutrons. Therefore, it is of interest to study quadrupole deformation and continuum effects on halo formation in B isotopes.

The continuum and particularly the resonant states in the continuum play a crucial role in the formation of exotic phenomena. Therefore, it is essential to reasonably handle the resonant states in the continuum, especially those near the threshold. Given the significance of resonant states in studying exotic phenomena, physicists have developed many theoretical resonance models, such as the Green's function method [46], the complex scaling method (CSM) [47], and the complex momentum representation (CMR) method [48].

To study the halo phenomenon, we used the CMR method based on the coupled-channel approach to solve the equations of motion of the deformed nucleus. It is worth noting that the quadrupole–quadrupole force in the spherical mean field is included in the deformation mean field and would make the single-particle figure work much better in the deformation nucleus than in the spherical nucleus. To determine the appearance of the halo phenomenon more accurately, it is essential to use models in which the radial wavefunctions of the weakly bound particles are treated appropriately in this study.

The CMR method can be used to obtain the bound states, resonant states, and continuum on an equal basis [48, 49]. This method is not only very effective for narrow resonances but also can be reliably applied to broad resonances. In particular, the results of the calculations have been proven to be independent of any nonphysical parameters, which ensures that high-precision energies and widths can be obtained. The CMR method is widely used to study the properties of weakly bound nuclei [50, 51]. We have recently studied in detail the structures of exotic spherical nuclei using the CMR method combined with the relativistic meson exchange model [48, 52] and relativistic point coupling model [53]. Furthermore, pairing correlations are treated with the BCS approximation, coupling bound states to resonant states and describing exotic phenomena such as halos and giant halos very well [54, 55].

In addition, we extended the CMR method to a deformed system. We have systematically investigated experimentally discovered and undiscovered halo structures, establishing that ^{31}Ne [50], ^{37}Mg [49], ^{53}Ar [56], ^{34}Na [57], and ^{29,31}F [58, 59] (or *s* waves or a mixture of *s* and *p* waves) are *p*-wave halo nuclei and that ^{19}C [60], ^{75}Cr [56], and ^{77}Fe [56] are *s*-wave halo nuclei. Recently, Wang et al. investigated neutron-rich ^{75}Cr using the CMR method in a relativistic mean-field framework, which applies to deformed nuclei. They found that ^{75}Cr is a *d*-wave deformed halo nucleus [61]. The ground-state properties of Ti isotopes were also investigated using the relativistic mean-field framework CMR method [62]. The predictions of halo phenomena in the neutron-rich region close to the neutron dripline will help to experimentally

explore the deformation halos of more nuclei in medium-mass regions. The present research demonstrates the advantages of the CMR method, which will help us explore further deformed halo nuclei using the CMR method.

In this study, we systematically investigated the exotic phenomena of ^{15,17,19}B using the CMR method. The energies and widths of the single-particle bound and resonant states, component ratios of the orbitals occupied by valence neutrons, and radial density distribution were obtained. The results revealed that ^{17,19}B may be prolate halo nuclei, which can be well understood because of the neutron halo phenomenon. In other words, observing the halo phenomena in ^{17,19}B can be used as critical evidence for the prolate deformation of ^{17,19}B ground states. The theoretical formalism is described in Sect. 2. Numerical details and results are presented in Sect. 3. Finally, a summary is provided in Sect. 4.

2 Formalism

We briefly introduce the theoretical framework of the CMR method to explore the ground-state properties of neutron-rich nuclei. The details of the CMR method can be found in Refs. [48, 50]. The main formulas of the CMR method are provided for the convenience of later discussion. We introduce a theoretical framework using the Hamiltonian

$$H = T + V, \tag{1}$$

where $T = \vec{p}^{\,2}/2m$ denotes the kinetic operator with momentum $\vec{p} = \hbar\vec{k}$ (where $\vec{k}$ is the wavevector). Following Ref. [63], the interaction potential V consists of the central potential, deformation potential, and spin-orbit coupling potential:

$$\begin{aligned} V_{\rm cent}(r) &= V_0(r), \\ V_{\rm def}(\vec{r}) &= -\beta_2 V_0 r \frac{{\rm d}f(r)}{{\rm d}r} Y_{20}(\vartheta,\varphi), \\ V_{\rm sl}(r) &= -16 V_0 \Lambda^2 \frac{1}{r}\frac{{\rm d}f(r)}{{\rm d}r}(\vec{s}\cdot\vec{l}), \end{aligned} \tag{2}$$

where Λ is the reduced Compton wavelength of the nucleon, $\hbar/m_{\rm r}c$, and

$$f(r) = \frac{1}{1+e^{\frac{r-R}{a}}}.$$

The diffuseness $a = 0.67$ fm, the radius $R = r_0 A^{1/3}$ with $r_0 = 1.27$ fm, and the depth of potential $V_0 = -51 + 33\frac{N-Z}{A}$ MeV depend on the mass number A, proton number Z, and neutron number N. To obtain the bound states, resonant states, and continuum on an equal footing, the Schrödinger equation is transformed from a coordinate representation to a momentum representation as

$$\int {\rm d}\vec{k}'\langle\vec{k}|H|\vec{k}'\rangle\psi(\vec{k}') = E\psi(\vec{k}), \tag{3}$$

where $\psi(\vec{k})$ are the momentum wavefunctions. For axially deformed nuclei, the third component of the total angular momentum Ω and parity π is good quantum numbers. The wavefunctions $\psi_\Omega(\vec{k})$ can be expanded as

$$\psi_\Omega(\vec{k}) = \sum_i \Phi_i(\vec{k}) = \sum_{lj} f^{lj}(k)\phi_{lj\Omega}(\Omega_k), \tag{4}$$

where $f^{lj}(k)$ and $\phi_{lj\Omega}(\Omega_k)$ are the radial and angular components, respectively. By substituting Eq. (4) into Eq. (3), the Schrödinger equation becomes

$$\begin{aligned} &\frac{\hbar^2k^2}{2M}f^{lj}(k) + \int k'^2{\rm d}k' V_s(l,j,k,k')f^{lj}(k') \\ &\quad - \beta_2\sum_{l'j'}\int k'^2{\rm d}k' V_d(l,j,l',j',m_j,k,k')f^{l'j'}(k') \\ &= Ef^{lj}(k), \end{aligned} \tag{5}$$

with

$$V_s(l,j,k,k') = \frac{2}{\pi}\int r^2{\rm d}r[V_{\rm cent}(r) + C_{\rm sl}V_{\rm sl}(r)]j_l(kr)j_l(k'r)$$

and

$$\begin{aligned} &V_d(l,j,l',j',\Omega,k,k') \\ &= i^{3l+l'}\frac{2}{\pi}\int r^2{\rm d}r k(r)j_l(kr)j_{l'}(k'r) \\ &\quad\cdot\sum_{m_s}\langle lm|Y_{20}(\Omega_r)|l'm\rangle\left\langle lm\frac{1}{2}m_s|j\Omega\right\rangle\left\langle l'm\frac{1}{2}m_s|j'\Omega\right\rangle. \end{aligned}$$

The above Schrödinger equation is solved in complex momentum space by diagonalizing the Hamiltonian matrix. For the sake of computational simplicity, the integral of Eq. (5) is transformed into summation form, and Eq. (5) becomes the matrix equation. In this study, it was combined with the coupled channel method to describe the deformed nuclei. Details can be found in Refs. [59, 60].

For every Nilsson level, the wavefunction is extended with a set of spherical components. The wavefunctions in the coordinate representation can be obtained using the following transformation:

$$\psi_\Omega(\vec{r}) = \frac{1}{(2\pi)^{3/2}}\int {\rm d}\vec{k}e^{i\vec{k}\cdot\vec{r}}\psi_\Omega(\vec{k}).$$

By assuming that $\psi_\Omega(\vec{r})$ holds the form

$$\psi_\Omega(\vec{r}) = \sum_{lj} f^{lj}(r)\phi_{lj\Omega}(\Omega_r), \tag{6}$$

where

$$f^{lj}(r) = i^l \sqrt{\frac{2}{\pi}} \sum_{a=1}^{N} \sqrt{w_a} k_a j_l(k_a r) \mathbf{f}^{lj}(k_a), \tag{7}$$

the corresponding radial density distributions can be calculated as

$$\rho(r) = \sum_{lj} f^{lj*}(r) f^{lj}(r). \tag{8}$$

3 Numerical details and results

The details of the numerical calculations are the same as those in Refs. [59, 60], where the number of coupling channels, N_c, momentum truncation maximum value k_{max}, and number of Gauss–Legendre grids, N_l are taken to be 8, 4.0 fm^{-1}, and 120, respectively. The CMR calculations achieved the required precision under these numerical conditions. Because quadrupole deformation and continuum effects play an essential role in the formation of the halo of exotic nuclei [35, 58, 64], the quadrupole deformation parameter β_2 was taken from −0.4 to 0.7 in steps of 0.02. Based on Refs. [48, 50], we found that the positions of the resonant states do not depend on the integration path. Therefore, we chose a sufficiently large contour ($k_1 = 0.0$ fm^{-1}, $k_2 = 0.5 - i0.5$ fm^{-1}, $k_3 = 1.0$ fm^{-1}, and $k_{max} = 4.0$ fm^{-1}) to expose all relevant resonances. Based on the numerical details presented, we first reveal the contributions of quadrupole deformations and continuum effects to the ground-state properties of ^{17}B.

The nuclear radius is a significant physical quantity that describes the exotic properties of nuclei. It is known that the root mean square (RMS) radius of halo nuclei (nuclei that form a halo away from the periphery of the core) increases suddenly compared to that of the neighboring nucleus. It can be seen from the definition of halo nuclei that the RMS radii of the orbits occupied by the last few valence neutrons are of crucial importance in researching halo phenomena. Therefore, we calculated the RMS radii for all the single-particle levels in the considered deformation range. For convenience, as shown in Fig. 1, we show only the RMS radii of the levels occupied by the last two valence neutrons of $^{13-19}$B for the quadrupole deformations $\beta_2 = -0.1$, 0.0, 0.1, 0.2, 0.3, 0.4, 0.5, 0.6, and 0.7.

The halo structure was experimentally confirmed for ^{17,19}B [19, 20]. The last two valence neutrons of ^{17}B occupy the levels 5/2[202], $1d_{5/2}$, 1/2[220], and 3/2[211] at $\beta_2 = -0.1$, $\beta_2 = 0.0$, $\beta_2 = 0.1$–0.2, and $\beta_2 = 0.3$–0.7, respectively (see Fig. 2). We can see that the RMS radius of level 3/2[211] occupied by the last two valence neutrons of ^{17}B significantly increases compared to that of ^{15}B at $\beta_2 = 0.6$ and $\beta_2 = 0.7$. However, we noticed that the

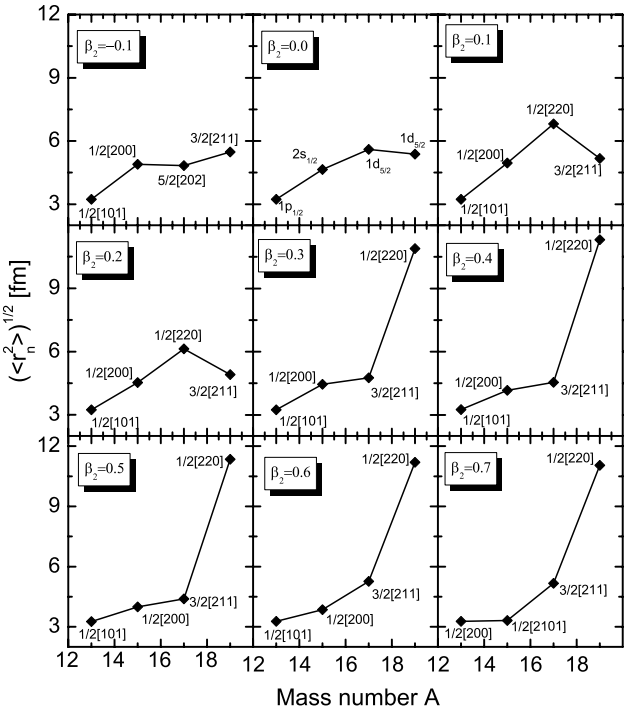

Fig. 1 (Color online) RMS radius of single-particle levels occupied by the last valence neutron as a function of the mass number A for $^{13-19}$B. The corresponding deformation β_2 and the quantum numbers of the level occupied by the last valence neutron are displayed in every subfigure

RMS radius of ^{17}B increases slightly at $\beta_2 = 0.1$–0.2, as a result of the valence neutrons occupying the resonant level 1/2[220]. This deformation region $\beta_2 = 0.1$–0.2 was excluded because ^{17}B is a weakly bound nucleus. Similar phenomena were observed in ^{19}B, where the RMS radius increased significantly compared to that of ^{17}B at $\beta_2 = 0.3$–0.7. For ^{15}B, there was no significant increase in the RMS radius over the range of deformations compared to the neighboring nuclei. Similar to the phenomena at $\beta_2 = 0.1$–0.2 in ^{17}B, the increased RMS radius for ^{15}B at $\beta_2 = -0.1$–0.2 is caused by the last two valence neutrons occupying an extremely weakly bound level 1/2[200]. However, the deformation region $\beta_2 = -0.1$–0.2 was excluded because the two-neutron separation energy of the weakly bound level 1/2[200] was much less than the experimental value of 3.747 MeV [33]. These phenomena suggest that ^{17}B and ^{19}B may be prolate halo nuclei with deformations $\beta_2 = 0.6$–0.7 and $\beta_2 = 0.3$–0.7, respectively. In comparison, ^{15}B is only a prolate deformation nucleus, which is relatively close to the results obtained from DRHBc calculations [35].

The neutron halo structure can be identified by analyzing the valence neutron levels. In Fig. 2, the Nilsson diagram of ^{17}B, including the resonant and bound levels,

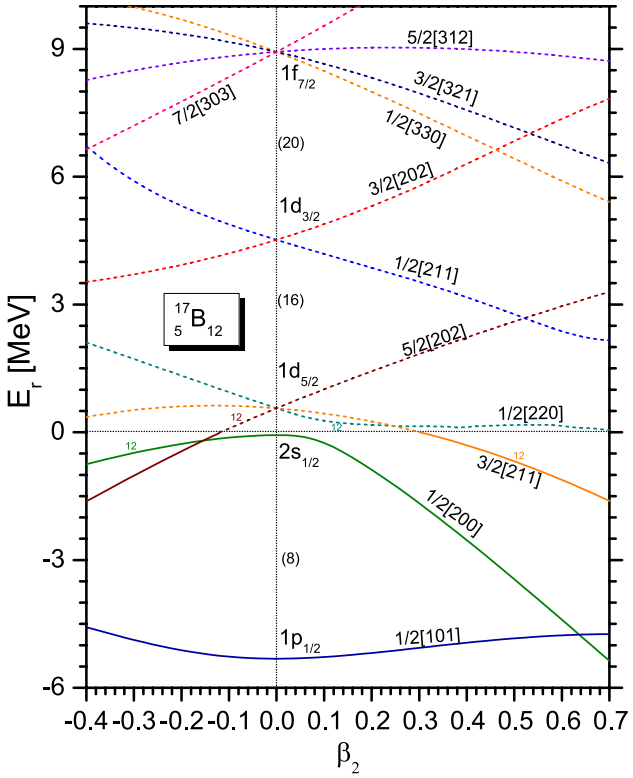

Fig. 2 (Color online) Neutron single-particle levels of ^{17}B as a function of β_2. Every Nilsson orbital is labeled with the quantum numbers $\Omega[Nn_z\Lambda]$. The bound and resonant levels are marked by solid and dashed lines, respectively

is shown to better study the effects of deformation and the continuum on halo structures. The bound and resonant states are marked with solid and dashed lines, respectively, and the corresponding Nilsson orbitals are marked with quantum numbers $\Omega[Nn_z\Lambda]$. Levels $1p_{1/2}$ and $2s_{1/2}$, and $1d_{5/2}$ and $1d_{3/2}$ have large shell gaps between them when spherical, that is, in the spherical case, the old magic number $N = 8$ is verified, and the new magic number $N = 16$ is suggested.

For the spherical configuration ($\beta_2 = 0$), level $2s_{1/2}$ is lower than $1d_{5/2}$, which means s–d orbitals are inverted compared to the level order in the stable nuclei. This is similar to the case of ^{17}B from DRHBc calculations [35]. In the spherical case, the resonant orbital $1d_{5/2}$ is occupied by the last two valence neutrons of ^{17}B, which have a large centrifugal barrier and negative two-neutron separation energy, suppressing the formation of halos. That is, the spherical shape does not support the formation of the halo phenomenon. Because the halo phenomena of ^{17}B have been observed experimentally [19], this suggests that ^{17}B is not a spherical nucleus but rather a deformed halo nucleus. Whether ^{17}B is a prolate or oblate deformation halo nucleus is an problem to be solved.

Driven by the deformation, the spherical levels split and the degenerate single-particle levels become undegenerated. We can see that some of these levels split off, some fall with deformation, and some rise with deformation. The resonant state $1d_{5/2}$ splits into Nilsson levels 1/2[220], 3/2[211], and 5/2[202], and the weakly bound level $2s_{1/2}$ becomes 1/2[200].

Nilsson levels 1/2[200], 5/2[202], 1/2[220], and 3/2[211] are occupied by the last two valence neutrons of ^{17}B at $-0.4 \le \beta_2 < -0.14$, $-0.14 \le \beta_2 < 0$, $0 < \beta_2 < 0.26$, and $0.26 \le \beta_2 \le 0.7$, respectively. Given that ^{17}B is a weakly bound nucleus, the last valence neutron may occupy the weakly bound level 1/2[200] with a deformation $-0.4 \le \beta_2 < -0.14$ or the weakly bound level 3/2[211] with a deformation $0.26 \le \beta_2 \le 0.7$.

On the oblate side, when pairing correlations are not considered, Nilsson level 1/2[200] is occupied by the last two valence neutrons of ^{17}B at $-0.4 \le \beta_2 < -0.14$. It should be indicated that the pairing correlations play important role at halo formation [65, 66]. Given the impact of pairing correlations, the last two neutrons can partially occupy level 1/2[200]. The two-neutron separation energies of the weakly bound level 1/2[200] are 0.75 MeV, which is much lower than the experimentally obtained value of 1.37 MeV [38]. This phenomenon suggests that ^{17}B is not an oblate nucleus.

In contrast, when pairing correlations are not considered, the Nilsson level 3/2[211] is occupied by the last two valence neutrons of ^{17}B at $0.26 \le \beta_2 \le 0.7$. The S_{2n} value of level 3/2[211] reaches 1.3–1.6 MeV with a deformation $0.6 \le \beta_2 \le 0.7$, which is close to the experimentally obtained 1.37 MeV [38] and, when combined with the analysis in Fig. 1, suggests that favorable conditions for halo formation are met in this deformation region. Given the impact of pairing correlations, the last two neutrons can partially occupy the level 3/2[211]. This implies that ^{17}B is a prolate deformation halo nucleus. This does not contradict the prediction of a prolate deformed halo nucleus for ^{17}B.

Figure 3 shows the widths of the single-particle resonant states in ^{17}B. For simplicity, the marks of the widths in Fig. 3 are the same as those for the levels shown in Fig. 2. Similar to the levels, there is a shell structure in the widths. Over the deformation range under consideration, the gap at $N = 16$ is relatively large, not only in a spherical shape but also in a deformed shape, which means that a new magic number $N = 16$ is supported in ^{17}B. The width of the resonant state 3/2[211] is consistently small and lies near zero potential energy. As β_2 increases, the width of resonant state 3/2[211] shrinks and the state eventually disappears, which is due to the resonance state 3/2[211] becoming a bound state. Therefore, it is relatively easy to form a halo at the level 3/2[211] in ^{17}B. The experimentally detected lifetime of ^{17}B will help us better understand the halo structure of ^{17}B because the widths are inversely proportional to the decay lifetime.

The above discussions indicate that the last two valence neutrons of ^{17}B occupy the Nilsson level 3/2[211] and

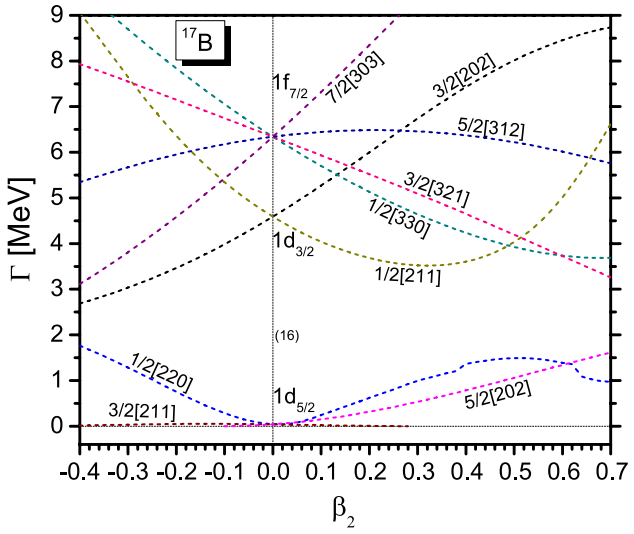

Fig. 3 (Color online) Same as Fig. 2, but for the widths for all the resonances of interest

that ^{17}B is a prolate halo nucleus with a deformation $0.6 \leq \beta_2 \leq 0.7$. To reveal the spherical component of the Nilsson orbitals occupied by the last valence neutron, the occupation probabilities of the level 3/2[211] are shown in Fig. 4. It can be seen that the configuration $d_{5/2}$ exceeds 90%. Configuration $d_{3/2}$ increases slowly, reaching ~ 6% at $\beta_2 > 0.62$. This suggests that the Nilsson level 3/2[211] is composed mainly of the d configuration, which is consistent with the results obtained in Ref. [67]. Meanwhile, the occupation probabilities of level 1/2[200] were plotted (and, as these are similar to those in Fig. 7, they are not shown here). The occupations of configurations $s_{1/2}$ and $d_{5/2}$ remain almost constant at $\beta_2 > 0.3$, both reaching ~ 47%, indicating that level 1/2[200] is mainly composed of configurations $d_{5/2}$ and $s_{1/2}$. This suggests that the occupation of level 1/2[200] makes an important contribution to the distribution of diffuse density in ^{17}B.

To better understand the effects of quadrupole deformation and single-particle levels occupied by valence neutrons on the halo structure, as shown in Fig. 5, we plotted the radial wavefunction for the 3/2[211] orbital at $\beta_2 = 0.64$. As in Fig. 4, the radial wavefunctions are shown only for the real part of the configurations $d_{3/2}$, $d_{5/2}$, $g_{7/2}$, and $g_{9/2}$. The other spherical components and the imaginary parts can be ignored. The dependence of the wavefunctions of configurations $d_{3/2}$ and $d_{5/2}$ ($l = 2$) on the radius r at long distances is not significantly different from that in the bound state. However, the wavefunctions of configurations $d_{3/2}$ and $d_{5/2}$ have large radial density distributions at $r \approx 3$ fm. It is well known that the d-wave configuration does not support the formation of halos owing to its large centrifugal potential barrier. Therefore, whether the halo phenomenon in ^{17}B occurs at $0.6 \leq \beta_2 \leq 0.7$ requires further exploration.

The exotic characteristic of the halo is its density distribution with a long tail compared to its neighboring levels. To check whether the levels 3/2[211] are occupied by the last two valence neutrons of ^{17}B at $0.6 \leq \beta_2 \leq 0.7$ is a reasonable approach. As shown in Fig. 6, we explored the density distribution of the single-particle orbital 3/2[211] at $\beta_2 = 0.64$. For comparison, the radial density distributions of levels 1/2[200] and 1/2[101] are also shown. The radial density distributions of the bound levels 1/2[200] and 1/2[101] did not diffuse at long distances. However, the weakly bound level 3/2[211] can be found trailing a longer tail at greater distances. According to Fig. 2,

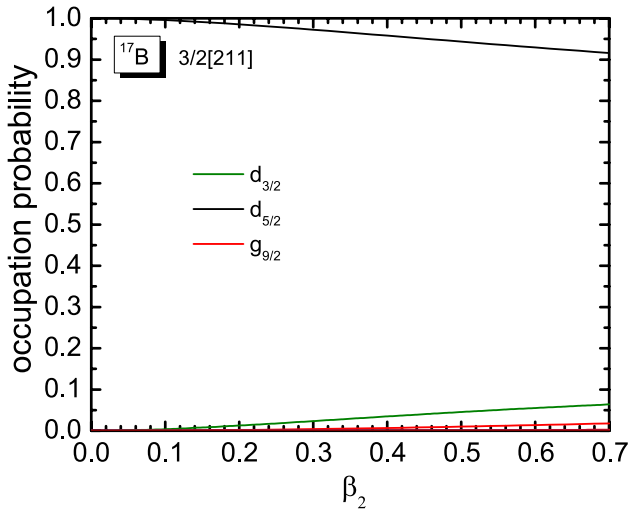

Fig. 4 (Color online) Occupation probabilities of major configurations as a function of β_2 for the single-particle level 3/2[211] in ^{17}B

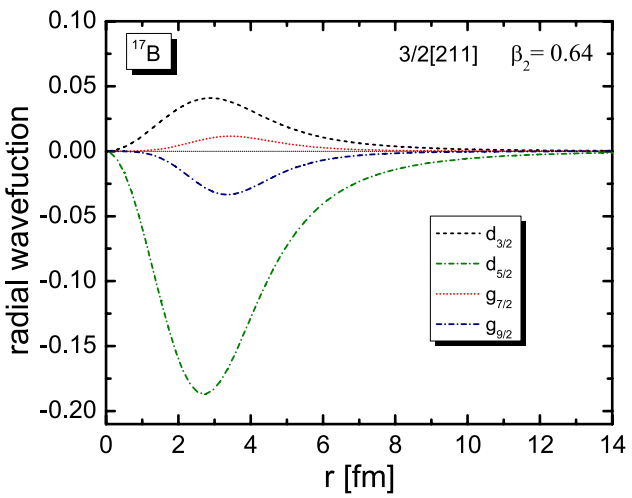

Fig. 5 (Color online) Wavefunctions of every component for the single neutron orbital 3/2[211] at $\beta_2 = 0.64$ for ^{17}B

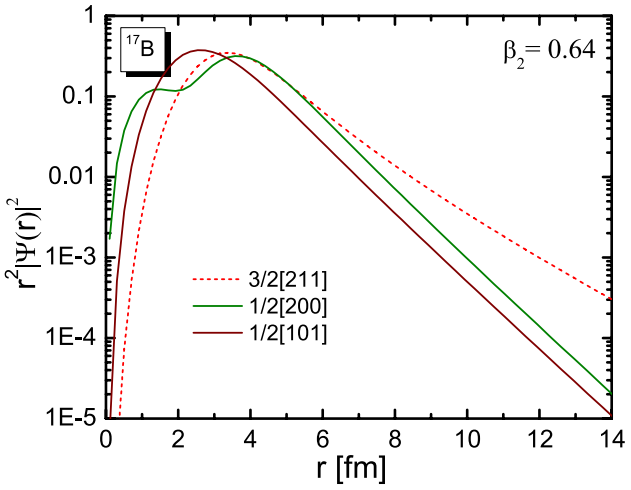

Fig. 6 (Color online) Radial density distributions multiplied by r^2 for the single-particle orbitals 3/2[211], 1/2[200], and 1/2[101] with $\beta_2 = 0.64$ in ^{17}B

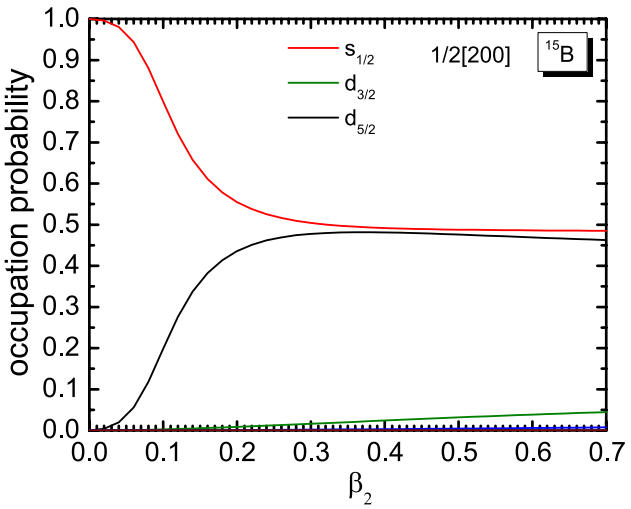

Fig. 7 (Color online) Same as Fig. 4, but for ^{15}B with the single-particle level 1/2[200]

we can see that the level 3/2[211] decreases slowly at $0.6 \leq \beta_2 \leq 0.7$. These phenomena indicate that the last two valence neutrons of ^{17}B occupy level 3/2[211] when $0.6 \leq \beta \leq 0.7$ and weak halo phenomena are observed. These results are consistent with the halo observed for ^{17}B [19]. In summary, the observed halo phenomena suggest that ^{17}B is a deformation halo nucleus with a deformation parameter $0.6 \leq \beta \leq 0.7$ and that its ground state consists mainly of the d configuration. However, we did not obtain the exact percentage of the $2s_{1/2}$ orbital, which also shows that the prerequisite for the occurrence of neutron halos is not the dominance of components with smaller orbital angular momentum.

The reliability of the CMR method for studying exotic phenomena is well demonstrated by investigating the halo structure in ^{17}B. Hence, to obtain the ground-state properties of the other neutron-rich B isotopes, we further explored the exotic structures of neutron-rich ^{15}B and ^{19}B using the CMR method.

Because ^{15}B has only two fewer neutrons than ^{17}B, the order of the single-particle levels does not change, except for a slight overall upward shift. When pairing correlations are not considered, as shown in Fig. 2, it can be seen that the last two valence neutrons of ^{15}B occupy levels 5/2[202] and 1/2[200], respectively. The S_{2n} value of the level 5/2[202] is 1.56 MeV at $\beta_2 \geq -0.4$, and the S_{2n} value of level 1/2[200] is 3.4 MeV and 4 MeV at $\beta_2 > 0.5$ and $\beta_2 < 0.56$, respectively, which is not in agreement with the experimentally obtained 3.747 MeV [33]. These phenomena suggest that ^{15}B may be a deformed nucleus, with β_2 between 0.5 and 0.56. Given the impact of pairing correlations, the last two neutrons can partially occupy level 1/2[200]. This does not contradict the prediction of a prolate deformed nucleus for ^{15}B.

To confirm the results obtained above, the occupation probabilities of levels 1/2[200] are plotted in Fig. 7. The occupations of configurations $s_{1/2}$ and $d_{5/2}$ decrease and increase rapidly with an increase in β_2, respectively. When $\beta_2 > 0.3$, their occupation remains almost constant, both reaching $\sim 50\%$, indicating that the level 1/2[200] is mainly composed of configurations $s_{1/2}$ and $d_{5/2}$.

As in Fig. 5, we show the radial wavefunction at $\beta_2 = 0.52$ for the single-particle orbital 1/2[200] of ^{15}B in Fig. 8. The wavefunction of configuration $s_{1/2}$ decreases gradually as r increases from 0 to 3 fm. The wavefunction of configuration $d_{5/2}$ has a large radial density distribution at $r \approx 3$ fm. As r increases further, the wavefunctions of configurations $s_{1/2}$ and $d_{5/2}$ converge rapidly to zero at long distances.

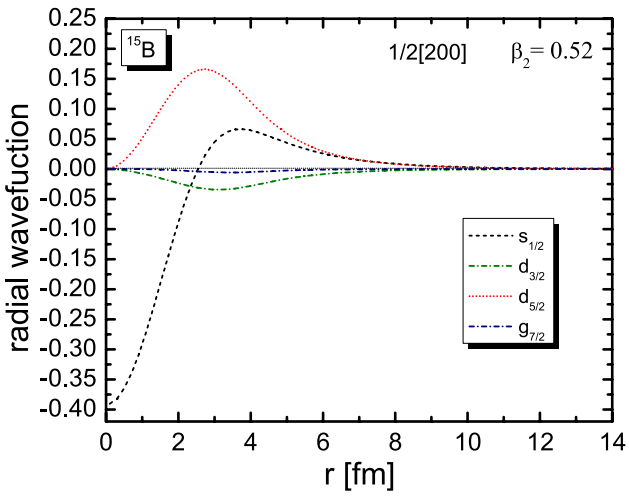

Fig. 8 (Color online) Same as Fig. 5, but for ^{15}B with the single-particle level 1/2[200]

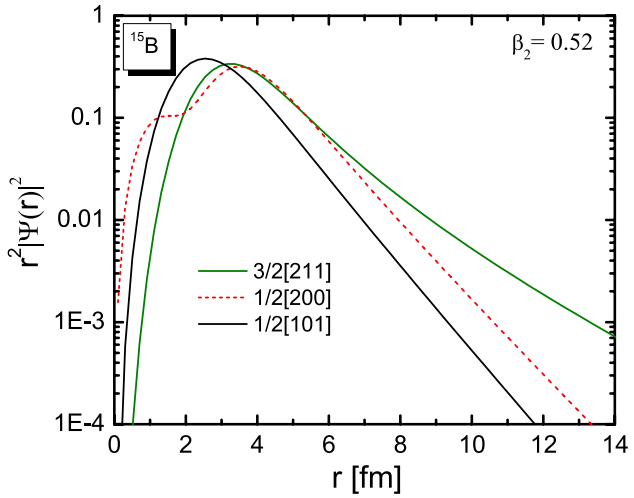

Fig. 9 (Color online) Same as Fig. 6, but for ^{15}B at $\beta_2 = 0.52$

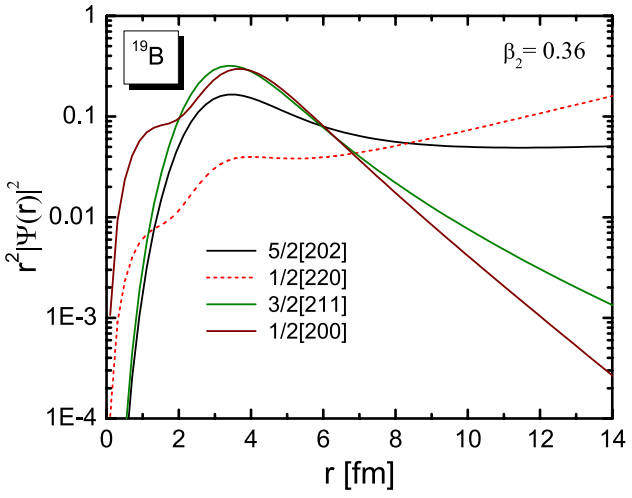

Fig. 10 (Color online) Same as Fig. 6, but for ^{19}B at $\beta_2 = 0.36$

Meanwhile, in Fig. 9, we plotted the density distributions of level 1/2[200] in ^{15}B at $\beta_2 = 0.52$. For comparison, we also show the density distribution for the 3/2[211] and 1/2[101] levels. The density distribution of the bound level 1/2[200] converges rapidly at longer distances, exhibiting no halo tails, suggesting that halo formation is not supported when the valence neutrons occupy level 1/2[200]. That is, ^{15}B is a prolate nucleus, but no halo phenomenon exists.

We performed a similar investigation on ^{19}B. Although ^{19}B has only two more neutrons than ^{17}B, the contribution of single-particle levels near the continuum threshold to the exotic phenomena becomes more significant, in addition to a slight downward shift at the single-particle level. This is consistent with the results obtained in Ref. [35] (in Fig. 2). When pairing correlations are not considered, the Nilsson levels 3/2[211], $1d_{5/2}$, 3/2[211], and 1/2[220] are occupied by the last two valence neutrons of ^{19}B. Given that ^{19}B is a weakly bound nucleus, the two-neutron separation energy is $0.089^{+0.560}_{-0.089}$ MeV [38]. Therefore, at $0.3 \leq \beta \leq 0.7$, level 1/2[220] can be occupied by the last two valence neutrons of ^{19}B. Given the impact of pairing correlations, the last two neutrons can partially occupy level 1/2[220]. This is not contradictory to the prediction of a prolate deformed halo nucleus for ^{19}B. However, whether halo phenomena appear in this deformation region requires further exploration.

To verify whether quadrupole deformation with $0.3 \leq \beta \leq 0.7$ is a reasonable conjecture in ^{19}B, we explore the density distribution of the single-particle orbital 1/2[220] at $\beta_2 = 0.36$ in Fig. 10. For comparison, the radial density distributions of levels 5/2[202], 3/2[211], and 1/2[200] are also shown. The radial density distributions of the bound levels 3/2[211] and 1/2[200] were not very diffuse at large distances. It is noteworthy that the level 1/2[220] has a larger diffuse density distribution than the resonant level 5/2[202]. These phenomena indicate that the last two valence neutrons of ^{19}B occupy level 1/2[220] when $0.3 \leq \beta \leq 0.7$ and halo phenomena are observed. These results are consistent with the observed halo [20] and the predicted deformation [35].

In addition, we also provide the occupation probabilities of level 1/2[220] in Fig. 11. This level consists mainly of the configurations $s_{1/2}$, $d_{3/2}$, and $d_{5/2}$, whereas the other configurations are negligible. Configuration $s_{1/2}$ is dominant compared to configurations $d_{3/2}$ and $d_{5/2}$. The occupation probability of configuration $s_{1/2}$ increases rapidly and then remains almost constant as β_2 increases, it still exceeds 65% on the prolate side, that is, the wavefunction of the weakly bound level 1/2[220] is composed mainly of configuration $s_{1/2}$, which supports the formation of the s-wave halo in ^{19}B.

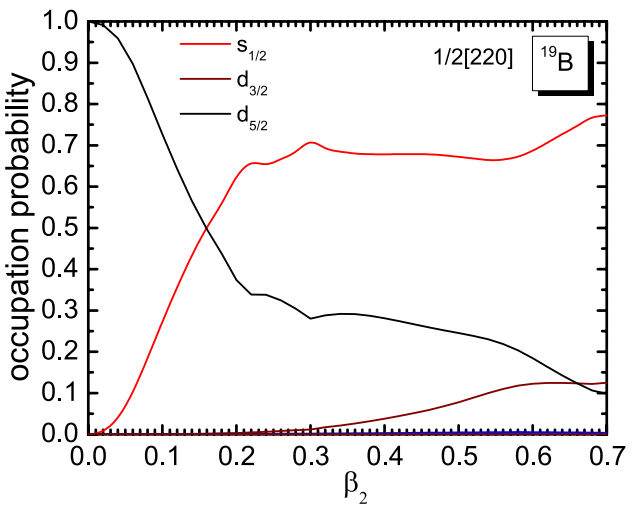

Fig. 11 (Color online) Same as Fig. 4, but for ^{19}B with the single-particle level 1/2[220]

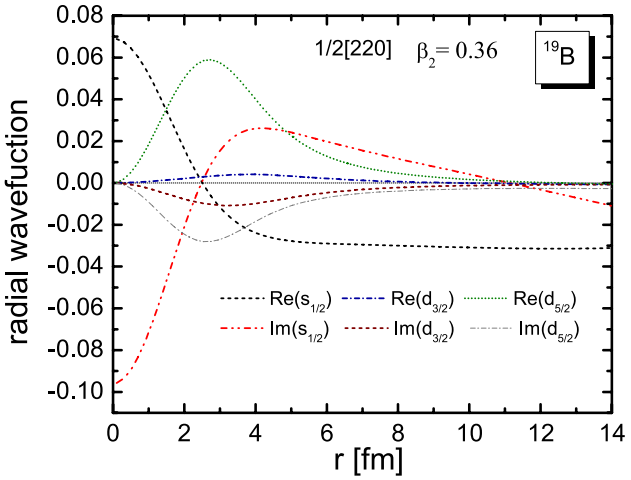

Fig. 12 (Color online) Same as Fig. 5, but for ^{19}B with the single-particle level 1/2[220]

To better understand the effect of single-particle levels with low orbital angular momentum on the halo structure, in Fig. 12, we plotted the radial wavefunction for orbital 1/2[220] at $\beta_2 = 0.36$. The radial wavefunctions are shown here only for the real and imaginary parts of configurations $s_{1/2}$, $d_{3/2}$, and $d_{5/2}$. The wavefunctions of the real and imaginary parts of the configuration $s_{1/2}$ ($l = 0$) extend to a considerable range in the coordinate space and exhibit significant halo phenomena. In contrast, the dependence of the wavefunctions of the real and imaginary parts of the configuration $d_{5/2}$ ($l = 2$) on radius r is not significantly different from that in the bound state. Although the wavefunctions of the real and imaginary parts of configuration $d_{5/2}$ have a large radial density distribution at $r \approx 3$ fm, these local wavefunctions do not support halo formation because of the large centrifugal potential barrier and small occupation probabilities. The halo phenomena observed in ^{19}B suggest that ^{19}B is a deformation halo nucleus with a deformation parameter $0.3 \leq \beta \leq 0.7$ and that it is the ground state consisting mainly of the s configuration.

The present method allows us to identify ^{15}B as a possible prolate nucleus with β_2 between 0.50 and 0.56, and the halo phenomena in ^{17}B and ^{19}B may occur at quadrupole deformations $0.6 \leq \beta_2 \leq 0.7$ and $0.3 \leq \beta \leq 0.7$, respectively. The above results indicate that the presence of ^{17}B and ^{19}B halo structures can be qualitatively explained in a valid model that considers quadrupole deformation and continuum spectral effects, despite its various limitations. The ground-state structures of ^{15}B are mainly the result of a certain degree of deformation. However, the ground-state structures of ^{17}B and ^{19}B are primarily the result of the interaction between s and d orbitals, large quadrupole deformation, and continuum effects.

4 Summary

Inspired by the recently reported experimental work on the halo phenomena in ^{17,19}B [19, 20], the role of quadrupole deformation and continuum effects on the halo structure of ^{17}B was studied using the CMR method.

Single-particle orbitals, including the bound and resonant states, were obtained, and an inversion of the s–d orbitals was found to be a critical factor in yielding the halo phenomena. At $\beta_2 = 0$, the neutron orbital $2s_{1/2}$ is lower than that of $1d_{5/2}$, and the valence neutrons are mainly dominated by the d wave. Therefore, ^{17}B is not a spherical nucleus. Driven by the deformation, the ground state of ^{17}B is prolate ($0.6 \leq \beta_2 \leq 0.7$) and a halo appears. The calculated occupation probabilities, radial density distributions, and wavefunctions support the results obtained by using the Nilsson levels. This indicates that the ground state of ^{17}B is a prolate halo nucleus, with $0.6 \leq \beta_2 \leq 0.7$.

As shown in Figs. 7, 8, 9, 10, 11 and 12, the ground state of ^{15}B also exhibits a large deformation but no halo phenomenon. By observing the radial density distribution and the configurations of the orbitals occupied by the valence neutrons, we find that the ground state of ^{19}B appears as halos at $0.3 \leq \beta_2 \leq 0.7$ and that the ground state consists mainly of the s configuration.

In this study, we used the CMR method to present some basic physics in a simple manner. By studying the quadrupole deformation and continuum effects in the ground-state properties of ^{15}B, ^{17}B, and ^{19}B, we found that the ground-state structure in ^{15}B may be significantly influenced by deformation effects and that the halo structures in ^{17,19}B may result from the interaction between s–d orbital reversals, large quadrupole deformations, and continuum effects. This work shows that further exploration of the relationship among halo features, deformation effects, and coupling of continuum spectra in more exotic nuclei is essential and interesting. Furthermore, the development of a CMR model is important, and future work will consider pairing correlations in this theoretical formalism.

Acknowledgements The authors are indebted to Jian-You Guo and Tai-Hua Heng for their constructive guidance and valuable suggestions.

Author contributions All authors contributed to the study conception and design. Material preparation, data collection and analysis were performed by Xue-Neng Cao, Xian-Xian Zhou, Ming Fu and Xin-Xing Shi. The first draft of the manuscript was written by Xue-Neng Cao and all authors commented on previous versions of the manuscript. All authors read and approved the final manuscript.

References

1. W. Nan, B. Guo, C.J. Lin et al., First proof-of-principle experiment with the post-accelerated isotope separator online beam at BRIF: measurement of the angular distribution of ^{23}Na + ^{40}Ca elastic scattering. Nucl. Sci. Tech. **32**, 53 (2021). https://doi.org/10.1007/s41365-021-00889-9
2. Z.P. Gao, Y.J. Wang, H.L. Lü et al., Machine learning of nuclear mass. Nucl. Sci. Tech. **32**, 109 (2021). https://doi.org/10.1007/s41365-021-00889-9
3. L. Zhou, S.M. Wang, D.Q. Fang et al., Recent progress in two-proton radioactivity measurement. Nucl. Sci. Tech. **33**, 105 (2022). https://doi.org/10.1007/s41365-022-01091-1
4. S.W. Bai, X.F. Yang, S.J. Wang et al., Commissioning of high-resolution collinear laser spectroscopy apparatus with laser ablation ion source. Nucl. Sci. Tech. **33**, 9 (2022). https://doi.org/10.1007/s41365-022-00992-5
5. I. Tanihata, H. Hamagaki, O. Hashimoto et al., Measurements of interaction cross-sections and nuclear radii in the light *p*-Shell Region. Phys. Rev. Lett. **55**, 2676 (1985). https://doi.org/10.1103/PhysRevLett.55.2676
6. P.G. Hansen, B. Jonson, The neutron halo of extremely neutron-rich nuclei. Europhys. Lett. **4**, 409 (1987)
7. J. Meng, H. Toki, S. Zhou et al., Relativistic continuum Hartree Bogoliubov theory for the ground-state properties of exotic nuclei. Prog. Part. Nucl. Phys. **57**, 470–563 (2006). https://doi.org/10.1016/j.ppnp.2005.06.001
8. T.T. Sun, L. Qian, C. Chen et al., Green's function method for the single-particle resonances in a deformed Dirac equation. Phys. Rev. C **101**, 014321 (2020). https://doi.org/10.1103/PhysRevC.101.014321
9. T. Minamisono, T. Ohtsubo, I. Minami et al., Proton halo of ^{8}B disclosed by its giant quadrupole moment. Phys. Rev. Lett. **69**, 2058 (1992). https://doi.org/10.1103/PhysRevLett.69.2058
10. T. Aumann, D. Aleksandrov, L. Axelsson et al., Continuum excitations in ^{6}H. Phys. Rev. C **59**, 1252 (1999). https://doi.org/10.1103/PhysRevC.59.1252
11. J. Wang, A. Galonsky, J.J. Kruse et al., Dissociation of ^{6}H. Phys. Rev. C **65**, 034306 (2002). https://doi.org/10.1103/PhysRevC.65.034306
12. T. Nakamura, A.M. Vinodkumar, T. Sugimoto et al., Observation of strong low-lying $E1$ strength in the two-neutron halo nucleus ^{11}Li. Phys. Rev. Lett. **96**, 252502 (2006). https://doi.org/10.1103/PhysRevLett.96.252502
13. Y. Kondo, T. Nakamura, Y. Satou et al., Low-lying intruder state of the unbound nucleus ^{13}B. Phys. Lett. B **690**, 245 (2010). https://doi.org/10.1016/j.physletb.2010.05.031
14. A. Corsi, Y. Kubota, J. Casal et al., Structure of ^{13}Be probed via quasi-free scattering. Phys. Lett. B **797**, 134843 (2019). https://doi.org/10.1016/j.physletb.2019.134843
15. I. Tanihata, T. Kobayashi, O. Yamakawa et al., Measurement of interaction cross sections using isotope beams of Be and B and isospin dependence of nuclear radii. Phys. Lett. B **206**, 592 (1985). https://doi.org/10.1016/0370-2693(88)90702-2
16. M. Fukuda, T. Ichihara, N. Inabe et al., The neutron halo in ^{11} is studied via reaction cross sections. Phys. Lett. B **268**, 339 (1991). https://doi.org/10.1016/0370-2693(91)91587-L
17. K. Tanaka, T. Yamaguchi, T. Suzuki et al., Observation of a large reaction cross-section in the rip-Line nucleus ^{22}C. Phys. Rev. Lett. **104**, 062701 (2010). https://doi.org/10.1103/PhysRevLett.104.062701
18. Y. Togano, T. Nakamura, Y. Kondo et al., Interaction cross-section study of the two-neutron halo nucleus ^{22}C. Phys. Lett. B **761**, 412 (2016). https://doi.org/10.1016/j.physletb.2016.08.062
19. Z.H. Yang, Y. Kubota, A. Corsi et al., Quasifree neutron knockout reaction revealed a small *s*-orbital component in the Borromean nucleus ^{17}B. Phys. Rev. Lett. **126**, 082501 (2021). https://doi.org/10.1103/PhysRevLett.126.082501
20. K.J. Cook, T. Nakamura, Y. Kondo et al., Halo structure of the neutron-dripline nucleus ^{19}B. Phys. Rev. Lett. **124**, 212503 (2020). https://doi.org/10.1103/PhysRevLett.124.212503
21. N. Kobayashi, T. Nakamura, Y. Kondo et al., Observation of a *p* -wave one-neutron halo configuration in ^{37}Mg. Phys. Rev. Lett. **112**, 242501 (2014). https://doi.org/10.1103/PhysRevLett.112.242501
22. T. Nakamura, N. Kobayashi, Y. Kondo et al., Deformation-driven p-wave halos at the drip line: ^{31}Ne. Phys. Rev. Lett. **112**, 142501 (2014). https://doi.org/10.1103/PhysRevLett.112.142501
23. S. Bagchi, R. Kanungo, Y.K. Tanaka et al., The two-neutron halo is unveiled in ^{29}F. Phys. Rev. Lett. **124**, 222504 (2020). https://doi.org/10.1103/PhysRevLett.124.222504
24. I. Tanihata, H. Savajols, R. Kanungo, Recent experimental progress in nuclear halo structure studies. Prog. Part. Nucl. Phys. **68**, 215 (2013). https://doi.org/10.1016/j.ppnp.2012.07.001
25. S.G. Zhou, J. Meng, P. Ring et al., Neutron halo in deformed nuclei. Phys. Rev. C **82**, 011301(R) (2010). https://doi.org/10.1103/PhysRevC.82.011301
26. X.X. Sun, J. Zhao, S.G. Zhou, Shrunk halo and quenched shell gap at $N = 16$ in ^{22}C: inversion of *sd*. Phys. Lett. B **785**, 530 (2018). https://doi.org/10.1016/j.physletb.2018.08.071
27. H.W. Hammer, L. Platter, Efimov states in nuclear and particle physics. Ann. Rev. Nucl. Part. Sci. **60**, 207 (2010). https://doi.org/10.1146/annurev.nucl.012809.104439
28. G. Hagen, P. Hagen, H.W. Hammer et al., Efimov physics around the neutron-rich ^{60}Ca isotope. Phys. Rev. Lett. **111**, 132501 (2013). https://doi.org/10.1103/PhysRevLett.111.132501
29. I. Hamamoto, Examining possible neutron-halo nuclei heavier than ^{37}Mg. Phys. Rev. C **95**, 044325 (2017). https://doi.org/10.1103/PhysRevC.95.044325
30. D. Hove, E. Garrido, P. Sarriguren et al., Emergence of clusters: halos, Efimov states, and experimental signals. Phys. Rev. Lett. **120**, 052502 (2018). https://doi.org/10.1103/PhysRevLett.120.052502
31. T. Suzuki, R. Kanungo, O. Bochkarev et al., Nuclear radii of ^{17,19}B and ^{14}Be. Nucl. Phys. A **658**, 313 (1999). https://doi.org/10.1016/S0375-9474(99)00376-0
32. T. Suzuki, Y. Ogawa, M. Chiba et al., Momentum distribution of ^{15}B fragments from the breakup of ^{17}B. Phys. Rev. Lett. **89**, 012501 (2002). https://doi.org/10.1103/PhysRevLett.89.012501
33. National Nuclear Data Center. http://www.nndc.bnl.gov
34. Y. Kondo, T. Nakamura, N. Aoi et al., In-beam γ-ray spectroscopy of neutron-rich boron isotopes ^{15,17}B via inelastic scattering at ^{12}C. Phys. Rev. C **71**, 044611 (2005). https://doi.org/10.1103/PhysRevC.71.044611
35. X.X. Sun, Deformed two-neutron halo in ^{19}B. Phys. Rev. C **103**, 054315 (2021). https://doi.org/10.1103/PhysRevC.103.054315
36. E. Sauvan, F. Carstoiu, N.A. Orr et al., One-neutron removal reactions on light neutron-rich nuclei. Phys. Rev. C **69**, 044603 (2004). https://doi.org/10.1103/PhysRevC.69.044603
37. Y. Yamaguchi, C. Wu, T. Suzuki et al., Density distribution of ^{17}B from the reaction cross-section measurement. Phys. Rev. C **70**, 054320 (2004). https://doi.org/10.1103/PhysRevC.70.054320
38. M. Wang, G. Audi, F. Kondev et al., AME2016 atomic mass evaluation (II). Tables, graphs, and references. Chin. Phys. C **41**, 030003 (2017). https://doi.org/10.1088/1674-1137/41/3/030003
39. Z. Dombrádi, Z. Elekes, R. Kanungo et al., Decoupling of valence neutrons from the core in ^{17}B. Phys. Lett. B **621**, 81 (2005). https://doi.org/10.1016/j.physletb.2005.06.031

40. A. Estradé, R. Kanungo, W. Horiuchi et al., Proton radii of $^{12-17}$B define a thick neutron surface in ^{17}B. Phys. Rev. Lett. **113**, 132501 (2014). https://doi.org/10.1103/PhysRevLett.113.132501
41. A. Ozawa, T. Suzuki, I. Tanihata, Nuclear size and related topics. Nucl. Phys. A **693**, 32 (2001). https://doi.org/10.1016/S0375-9474(01)01152-6
42. H.T. Fortune, R. Sherr, Matter radii and wave function admixtures in 2n halo nuclei. Eur. Phys. J. A **48**, 103 (2012). https://doi.org/10.1140/epja/i2012-12103-9
43. Y. Kanada-En'yo, H. Horiuchi, Neutron-rich B isotopes studied with antisymmetrized molecular dynamics. Phys. Rev. C **52**, 647 (1995). https://doi.org/10.1103/PhysRevC.52.647
44. Y. Kanada-En'yo, H. Horiuchi, Structure of light unstable nuclei studied with antisymmetrized molecular dynamics. Prog. Theor. Phys. Suppl. **142**, 205 (2001). https://doi.org/10.1143/PTPS.142.205
45. L. Gaudefroy, W. Mittig, N.A. Orr et al., Direct mass measurements of ^{19}B, ^{22}C, ^{29}F, ^{31}Ne, ^{34}Na, and other light-exotic nuclei. Phys. Rev. Lett. **109**, 202503 (2012). https://doi.org/10.1103/PhysRevLett.109.202503
46. Y.T. Wang, T.T. Sun, Searching for single-particle resonances with the Greens function method. Nucl. Sci. Tech. **32**, 46 (2021). https://doi.org/10.1007/s41365-021-00884-0
47. X.X. Shi, M. Shi, Z.M. Niu et al., Probing resonances in deformed nuclei using the complex-scaled Green's function method. Phys. Rev. C **94**, 024302 (2016). https://doi.org/10.1103/PhysRevC.94.024302
48. N. Li, M. Shi, J.Y. Guo et al., Probing resonances of the Dirac equation with complex momentum representation. Phys. Rev. Lett. **117**, 062502 (2016). https://doi.org/10.1103/PhysRevLett.117.062502
49. Z. Fang, M. Shi, J.Y. Guo et al., Probing resonances in the Dirac equation with quadrupole-deformed potentials using a complex momentum representation method. Phys. Rev. C **95**, 024311 (2017). https://doi.org/10.1103/PhysRevC.95.024311
50. Y.J. Tian, Q. Liu, T.H. Heng et al., Research on halo in ^{31}Ne using the complex momentum representation method. Phys. Rev. C **95**, 064329 (2017). https://doi.org/10.1103/PhysRevC.95.064329
51. K.M. Ding, M. Shi, J.Y. Guo et al., Resonant-continuum relativistic mean field plus BCS in a complex momentum representation. Phys. Rev. C **98**, 014316 (2018). https://doi.org/10.1103/PhysRevC.98.014316
52. M. Shi, Z.M. Niu, H.Z. Liang, Combination of complex momentum representation and Green's function methods in the relativistic mean-field theory. Phys. Rev. C **97**, 064301 (2018). https://doi.org/10.1103/PhysRevC.97.064301
53. Y. Wang, Z.M. Niu, M. Shi et al., Probing the resonance of Dirac particles in the relativistic point-coupling model using the complex momentum representation method. J. Phys. G **46**, 125103 (2019). https://doi.org/10.1088/1361-6471/ab4a9b
54. X.N. Cao, Q. Liu, Z.M. Niu et al., Systematic studies of the influence of single-particle resonances on neutron halo and skin in the relativistic-mean-field and complex-momentum-representation methods. Phys. Rev. C **99**, 024314 (2019). https://doi.org/10.1103/PhysRevC.99.024314
55. X.N. Cao, M. Fu, X.X. Zhou et al., Research on the exotic properties of nuclei from light to medium mass regions. Eur. Phys. J. Plus **137**, 906 (2022). https://doi.org/10.1140/epjp/s13360-022-03
56. X.N. Cao, Q. Liu, J.Y. Guo, Prediction of halo structure in nuclei heavier than ^{37}Mg with the complex momentum representation method. Phys. Rev. C **99**, 014309 (2019). https://doi.org/10.1103/PhysRevC.99.014309
57. Y.X. Luo, Q. Liu, J.Y. Guo et al., Investigation of the exotic structure in ^{34}Na using complex momentum representation combined with Green's function method. J. Phys. G **47**, 085105 (2020). https://doi.org/10.1088/1361-6471/ab92e2
58. Y.X. Luo, Q. Liu, J.Y. Guo, Role of quadrupole deformation and continuum effects in the "island of inversion'' nuclei ^{28,29,31}F. Phys. Rev. C **104**, 014307 (2021). https://doi.org/10.1103/PhysRevC.104.014307
59. S.Y. Zhai, X.N. Cao, J.Y. Guo, Research on the deformed halo in ^{29}F with complex momentum representation method. J. Phys. G **49**, 065101 (2022). https://doi.org/10.1088/1361-6471/ac5dfd
60. X.N. Cao, Q. Liu, J.Y. Guo, Interpretation of halo in ^{19}C with complex momentum representation method. J. Phys. G **45**, 085105 (2018). https://doi.org/10.1088/1361-6471/aad0bf
61. X.W. Wang, J.Y. Guo, Research on deformed exotic nuclei by relativistic mean field theory in complex momentum representation. Phys. Rev. C **104**, 044315 (2021). https://doi.org/10.1103/PhysRevC.104.044315
62. T.H. Heng, Y.W. Chu, Properties of Titanium isotopes in complex momentum representation within relativistic mean-field theory. Nucl. Sci. Tech. **33**, 117 (2022). https://doi.org/10.1007/s41365-022-01098-8
63. I. Hamamoto, One-particle resonant levels in a deformed potential. Phys. Rev. C **72**, 024301 (2005). https://doi.org/10.1103/PhysRevC.72.024301
64. I. Hamamoto, Deformed halo of $^{29}_{9}F_{20}$. Phys. Lett. B **814**, 136116 (2021). https://doi.org/10.1016/j.physletb.2021.136116
65. K. Bennaceur, J. Dobaczewski, M. Ploszajczak, Pairing anti-halo effect. Phys. Lett. B **496**, 154 (2000). https://doi.org/10.1016/S0370-2693(00)01292-2
66. H. Nakada, K. Takayama, Intertwined effects of pairing and deformation on neutron halos in magnesium isotopes. Phys. Rev. C **98**, 011301(R) (2018). https://doi.org/10.1103/PhysRevC.98.011301
67. T. Suzuki, T. Otsuka, Structure of two-neutron halo in light exotic nuclei. Few-Body Syst. **62**, 32 (2021). https://doi.org/10.1007/s00601-021-01612-5